nature photonics

ARTICLES

PUBLISHED ONLINE: 17 AUGUST 2015 | DOI: 10.1038/NPHOTON.2015.151

Role of microstructure in the electron–hole interaction of hybrid lead halide perovskites

Giulia Grancini[1†], Ajay Ram Srimath Kandada[1†], Jarvist M. Frost[2], Alex J. Barker[1], Michele De Bastiani[1,3], Marina Gandini[1,4], Sergio Marras[5], Guglielmo Lanzani[1,4], Aron Walsh[2] and Annamaria Petrozza[1*]

Organic–inorganic metal halide perovskites have demonstrated high power conversion efficiencies in solar cells and promising performance in a wide range of optoelectronic devices. The existence and stability of bound electron–hole pairs in these materials and their role in the operation of devices with different architectures remains a controversial issue. Here we demonstrate, through a combination of optical spectroscopy and multiscale modelling as a function of the degree of polycrystallinity and temperature, that the electron–hole interaction is sensitive to the microstructure of the material. The long-range order is disrupted by polycrystalline disorder and the variations in electrostatic potential found for smaller crystals suppress exciton formation, while larger crystals of the same composition demonstrate an unambiguous excitonic state. We conclude that fabrication procedures and morphology strongly influence perovskite behaviour, with both free carrier and excitonic regimes possible, with strong implications for optoelectronic devices.

Hybrid perovskites represent a new, disruptive technology in the field of optoelectronics. They have the potential to overcome the performance limits of current technologies while achieving low cost and high integrability. Hybrid halide perovskite (for example, $CH_3NH_3PbX_3$ [X = Cl, Br or I]) solar cells with power conversion efficiencies exceeding 20%[1,2] are effectively challenging existing thin-film technologies. In addition, the incorporation of hybrid perovskites in optical cavities as lasing materials[3–5] and in diode structures as efficient light emitters[6] demonstrates their flexibility and potential for technologically relevant applications beyond photovoltaics.

Hybrid perovskites are usually deposited as polycrystalline thin films with variable mesoscale morphology depending on the growth conditions, and the obtained grain size ranges from tens to thousands of nanometres[7–9]. Over the last two years the impressive improvement in photovoltaic performance has been driven by empirical evolution of the device architecture and processing methodologies. However, there is a considerable lack of understanding of material properties, both as pristine films and in their embodiment in a device. Early studies classified the working mechanism of perovskite based solar cells within a pure excitonic paradigm[10], with bound electron and hole pairs providing the primary photoexcitation. More recent investigations have put forward a different scenario, where photoexcitation leads mainly to the generation of free electrons and holes, similar to the case of conventional polycrystalline inorganic semiconductors[4,11–16]. Recently, there have been several reports on the optical properties of hybrid perovskite single crystals[17–19], which should provide a reliable reference state. However, even in this case, a few discrepancies are evident. For example, Shi and colleagues[17] report an optical absorption spectrum with onset at 1.63 eV and no sign of excitonic states[17], while Dong and co-workers[18] show evidence of a strong excitonic peak at the onset of the external quantum efficiency (EQE) spectrum, at 1.51 eV (ref. 18).

In this Article we describe the interplay between free carriers and excitons, based on transient absorption (TA) spectroscopy and multiscale numerical simulations. $CH_3NH_3PbI_3$ ($MAPbI_3$) crystallized in a mesoporous scaffold, with a small grain size (tens of nanometres), does not support exciton states even at low temperature. In contrast, in hundreds of nanometre-sized domains, as formed by deposition on a flat substrate, free carriers may thermalize and coalesce into the ‘exciton state’, depending on the temperature and excitation density. Similar behaviour is also observed for the higher-bandgap $CH_3NH_3PbBr_3$ ($MAPbBr_3$). Thus, a definitive classification—‘excitonic’ or ‘free carrier’ semiconductor—as well as a universal value for the exciton binding energy in semiconductors presenting the same chemical composition is not possible for hybrid perovskites as both regimes are physically accessible by appropriately processing the compounds. We rationalize this by introducing a model for dielectric screening in perovskites. Such a screening is possible due to the polarization of the medium, and can originate from electronic as well as lattice displacements. Here, we find it is strongly dependent on coherent long-range order in the lattice, which can be disrupted by imperfections such as domain walls within crystals or surface defects. As the permanent dipoles associated with the methylammonium cation are free to rotate within the inorganic cage of the hybrid perovskites, they contribute to lattice polarization, screening the electron–hole Coulomb interaction.

We first consider a $MAPbI_3$ film fabricated by two-step deposition on a 3-μm-thick alumina mesoporous scaffold, one of the most established architectures for efficient perovskite solar cells[20] (see Methods for details of sample preparation). This sample provides simultaneous access to two distinct structural morphologies: the crystalline phase grown within the scaffold (termed the ‘meso’ phase in the following) which, on average, limits the crystal size to the nanometre scale[7,9], and the

---

[1]Center for Nano Science and Technology @Polimi, Istituto Italiano di Tecnologia, via Giovanni Pascoli 70/3, Milan 20133, Italy. [2]Centre for Sustainable Chemical Technologies and Department of Chemistry, University of Bath, Claverton Down, Bath BA2 7AY, UK. [3]Dipartimento di Scienze Chimiche, Università degli Studi di Padova, via Marzolo 1, Padova 35131, Italy. [4]Dipartimento di Fisica, Politecnico di Milano, Piazza L. da Vinci, 32, 20133 Milano, Italy. [5]Department of Nanochemistry, Istituto Italiano di Tecnologia, via Morego 30, Genova 16163, Italy. †These authors contributed equally to this work. *e-mail: annamaria.petrozza@iit.it

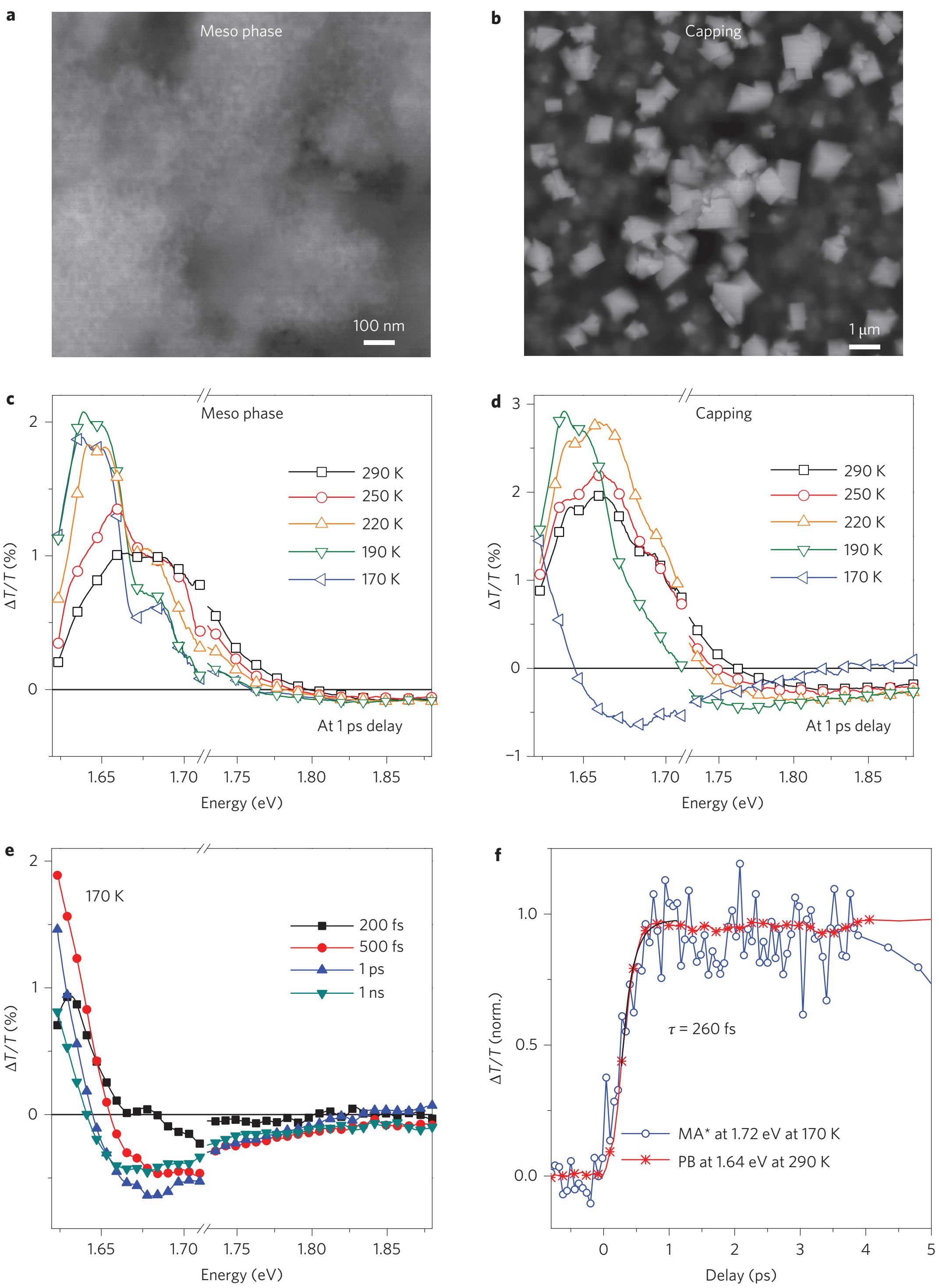

Figure 1 | Temperature-dependent transient absorption spectra of MAPbI$_3$ meso phase and capping layer. a,**b**, SEM images of the meso phase (**a**) and capping layer (**b**) of the 3-μm-thick MAPbI$_3$ sample. **c**, Temperature dependence of the TA spectra at 1 ps pump–probe delay of the meso phase. **d**, Temperature dependence of the TA spectra at 1 ps pump–probe delay of the capping layer. **e**, TA spectra between 200 fs and 1 ns at 170 K for the capping layer. **f**, Dynamics probed at 1.72 eV (MA* band) for the capping layer at 170 K compared to the dynamics probed at 1.64 eV (PB band) of the same sample at room temperature (290 K). For all TA measurements, the excitation wavelength was at 2.38 eV with an excitation density of ~5×10^{17} cm^{-3}.

thick capping layer on top of the scaffold, consisting of crystals up to hundreds of nanometres in size (Fig. 1a,b, respectively; for X-ray diffraction (XRD) analysis see Supplementary Fig. 1). The temperature-dependent optical absorption spectrum of such a sample is presented in Supplementary Fig. 2, and does not show any excitonic transition at the onset, similar to what we have previously reported[12].

In agreement with previous works[4,11,21], the TA spectra of the meso phase upon photoexcitation above the band-edge can be accounted for by considering the photo-induced charge-carrier dynamics, without invoking any excitonic contributions. Note that the sample was photoexcited from the substrate side in order to selectively interrogate the perovskite phase grown in the scaffold. At room temperature, the photo-bleach (PB) signal around 1.67 eV shows a rise with a time constant of 260 fs due to the hot-carrier thermalization to the band-edge and a broad photo-induced absorption (PA_1) band that forms for energies higher than 1.77 eV (refs 4,11,21). Briefly, the PB band is assigned to band filling of the free carriers, while PA_1 has been tentatively assigned in the literature to the change in refractive index induced by the free-carrier population (Supplementary Figs 3 and 4). Figure 1c shows that, on reducing the temperature (but still above the tetragonal-to-orthorhombic phase transition), the PB band redshifts, becomes narrower and gains intensity. The change in line shape is consistent with the lower thermal energy, which reduces homogeneous broadening. The redshift can be simply related to the Varshni effect[22] (for a discussion see Supplementary Fig. 5). It is worth underlining here that this sample does not show any excitonic peak in the absorption spectrum, even at 4 K (Supplementary Fig. 2b).

Figure 1d presents the temperature-dependent TA spectra of the same sample illuminated from the capping side. Because the pump photon penetration depth is comparable to the thickness of the capping layer, it is mainly the large crystals in the capping phase that are excited, although some contribution from the smaller crystals within the scaffold can be present (Fig. 1b). Note that the pump–probe signal is due to the photoexcited volume, and the unexcited regions, however large, do not contribute. Transmission of the probe through the unexcited volume of the sample is cancelled out in the transmission difference signal. At room temperature we note that the PB band is broader and redshifted with respect to the PB of the meso phase of the film. The redshift is due to the reduction of the bandgap in the large crystals[13], while the broadening can be related to contributions from the meso phase underneath. The most striking difference appears when the sample is cooled down. In particular, at 170 K, the PB band is strongly redshifted. Such a large redshift does not follow the standard Varshni trend. Furthermore, the PA_1 band is simultaneously quenched and a new negative band appears, peaking around 1.67 eV. Note that this is not simply related to the low-temperature structural phase transition that occurs below 170 K (refs 12,23), which would lead to a blueshift of the whole spectrum as a consequence of a widening of the semiconductor bandgap (Supplementary Figs 6 and 7).

The time evolution of the TA spectra at 170 K is shown in Fig. 1e. At 200 fs, a positive band peaking close to 1.63 eV is present. In ~1 ps ($\tau \approx 260$ fs) a negative band peaking at 1.67 eV forms together with the redshift of the PB, which falls outside our experimental range. Such a behaviour has been well documented in semiconductors as a result of self-normalization of the exciton energy (that is a blueshift of the exciton absorption) due to exciton–exciton and exciton–carrier interactions[24–28]. The negative band is therefore the result of a modulation (in the following we indicate it as MA*) and can be considered as a fingerprint for exciton population[24,26]. As previously asserted, large crystals show a clear excitonic transition at the absorption edge that gains strength upon cooling [7,12,29]. Even considering the lowest exciton binding energy reported so far in the literature (5 meV, refs 14,16,30), one can expect a significant exciton population at 170 K at the photoexcitation densities used (a simple guideline to estimate the exciton population fraction depending on the exciton binding energy value, temperature and excitation density is presented in Supplementary Fig. 8). Accordingly, at 170 K the formation of MA* is indicative of exciton formation upon carrier thermalization. We estimate that the carrier coalescence into the bound excitonic state occurs within 1 ps (dynamics in Fig. 1f), consistent with the similar phonon-assisted phenomenon that occurs in band relaxation. Note that in two-dimensional hybrid perovskites the formation of MA* has also been reported (although it is slower)[24,28].

In this specific morphology, the exciton population appears only with a reduction in temperature, implying that the exciton binding energy is insufficient to stabilize the exciton population at room temperature. To broaden the perspective of our observations we fabricated ‘cuboids-like’ films of $MAPbI_3$ (ref. 20), with controlled crystal dimensions of either <200 nm or ~1 μm (from visual inspection of scanning electron microscopy (SEM) images in Fig. 2a and b, respectively; see Supplementary Fig. 1 for XRD analysis). The UV–vis absorption spectra at room temperature are shown in Supplementary Fig. 9. The TA spectrum of the film with a crystal size of <200 nm (indicated in the legend of Fig. 2c as ‘Small crystals’) closely resembles the one obtained in the meso phase of the $MAPbI_3$ film at room temperature (for the TA spectra at 1 ps, after carrier thermalization, see Fig. 2c, and for the entire spectral dynamics see Supplementary Fig. 10). No exciton feature is present. On the contrary, the sample made of ~1 μm large crystals exhibits (at room temperature) different spectral features and dynamics. The TA spectrum forming in 1 ps upon photoexcitation above the bandgap resembles the one of the capping layer at 170 K (Fig. 2c). In particular we highlight the presence of the MA* band even at room temperature, with a formation time of ~270 fs (Fig. 2d, inset). Note that this sample keeps the same TA spectral features even at 77 K, where a clear stable excitonic state is also present at the band-edge (see the UV–vis spectra in Supplementary Fig. 6), albeit shifted to higher energies (~95 meV, see TA spectrum in Supplementary Fig. 7) as a consequence of a phase transition. Figure 2c shows the TA spectrum taken at 77 K (dashed line), shifted, and superimposed to the one taken at room temperature for easier comparison. This provides additional support to our assignment of the TA spectra and the correct prediction of a bleaching band just outside the experimental range. Figure 2d presents details of the spectral evolution of the sample with large crystals. Importantly, at longer time delays (>10 ps) the MA* band reduces and the PB shifts to higher energies, towards the free-carrier bleach. This dynamic reflects the decay of the excitonic population, which appears to be shorter-lived with respect to the free-carrier population, as further confirmed by the TA spectra in the nanosecond time regime (Supplementary Fig. 11).

We have shown so far that different morphologies of $MAPbI_3$ thin films (with average crystal sizes varying from tens to hundreds of nanometers) may (1) support only an electron hole plasma, even at low temperature; (2) support an excitonic population upon temperature reduction; and (3) sustain the formation of a fraction of short-lived excitons at room temperature. Because the photoexcitation density used in the above three cases is the same, this clearly indicates that the electron–hole interaction is modified by the degree of polycrystallinity in the film (see Supplementary Fig. 8 for a simple visualization of the variation of exciton population fraction as a function of exciton binding energy at a given photoexcitation density). Thus, the exciton binding energy is not uniquely determined by the chemical composition of the polycrystalline material, but can be tuned in a range between a few and tens of meV (refs 14–16).

To further generalize our observations we also consider thin films of $MAPbBr_3$. The halogen substitution induces a lowering of the valence band of the semiconductor and a blueshift of the optical gap, making the material appealing for a variety of applications such as high V_{oc} solar cells[31,32], water splitting and light-emitting devices[3,6]. Seminal studies have suggested a larger exciton binding energy for $MAPbBr_3$ compared to $MAPbI_3$[33]. However, the optical spectra reported by some recent works[32,34,35] do not show any strong excitonic feature at room temperature. To verify the role of morphology in this system we prepared $MAPbBr_3$ thin films with average crystal dimensions much smaller than 100 nm (by growing them in an Al_2O_3 mesoporous scaffold) and of approximately 1 μm (see SEM images in

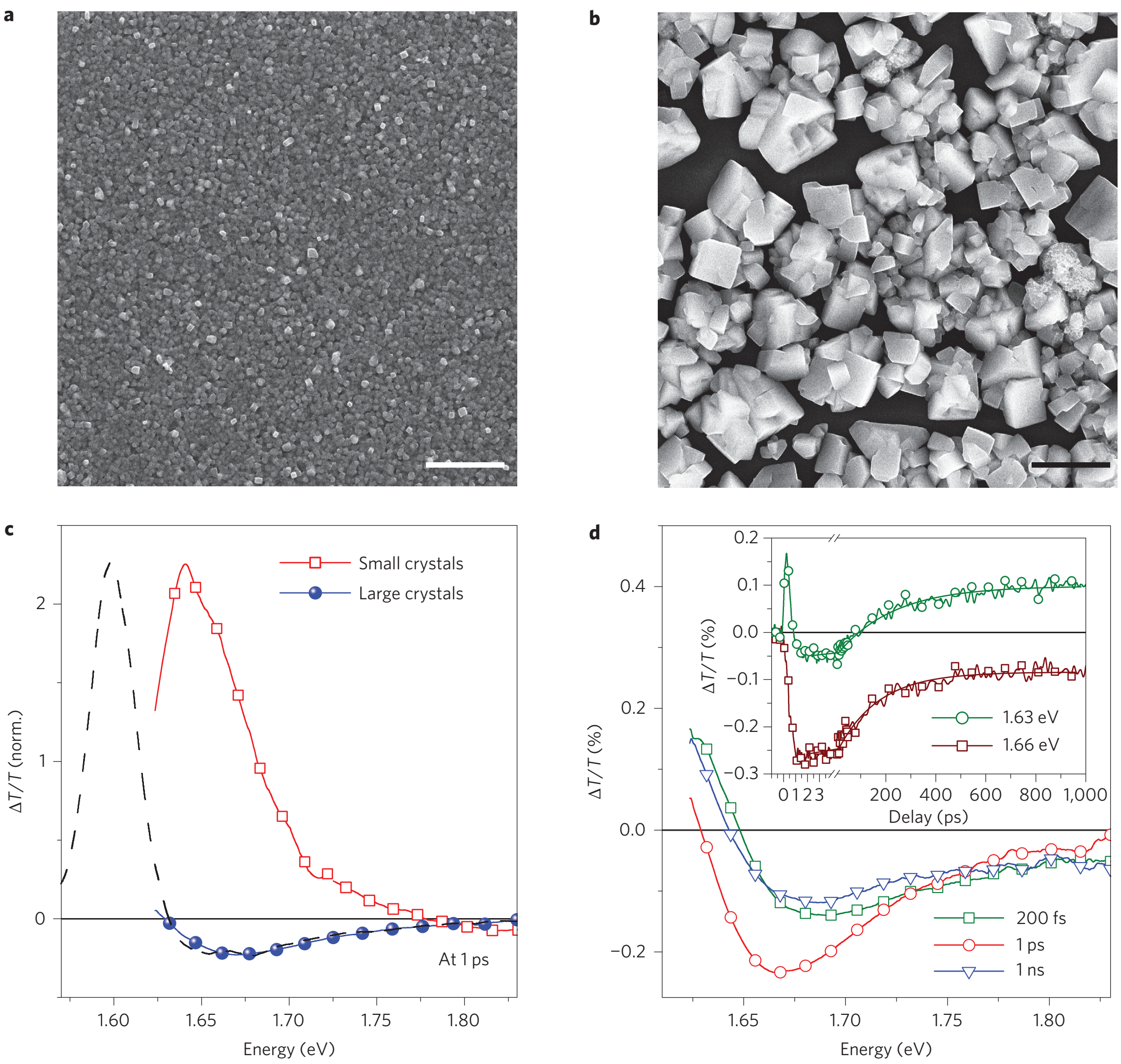

Figure 2 | Photo-induced excited population of MAPbI$_3$ as a function of crystal size. a,**b**, SEM images of perovskite films with average crystal dimensions of <200 nm (**a**) and ~1 µm (**b**). Scale bars, 2 µm. **c**, TA spectra at room temperature, at 1 ps pump–probe delay, of the two samples shown in **a** and **b** (red squares and blue circles, respectively) as well as the TA spectrum (dashed line) of the sample in **b**, taken at 77 K, redshifted by 95 meV. **d**, TA spectra at different time delays, at room temperature, from the sample shown in **b**. Inset: dynamics probed at 1.63 eV and 1.66 eV. For all TA measurements, the excitation wavelength is at 2.38 eV with an excitation density of ~5×10^{17} cm^{-3}.

Supplementary Fig. 12). Figure 3a,b shows the UV–vis spectra of such samples, and Fig. 3c,d shows the photo-induced TA spectra when exciting above bandgap at room temperature. Small crystals do not show any excitonic feature at the onset of the UV–vis absorption spectrum, at room temperature. In perfect agreement, in terms of its shape and dynamics, the TA spectrum resembles very much that from meso MAPbI$_3$, pointing to a free-carrier picture (Supplementary Figs 3 and 4). In contrast, large crystals show a sharp excitonic feature at the onset of the absorption spectrum (Fig. 3b). In agreement, the TA spectra (Fig. 3d) of the large MAPbBr$_3$ crystals show the formation of a PB band at 2.34 eV that matches the excitonic transition, together with the appearance of the modulation feature, MA*, at 2.43 eV in the first picosecond (a comparison of the 1 ps spectra from the small and the large crystal is reported in the inset of Fig. 3d). This behaviour indicates the formation of an exciton population upon carrier thermalization that eventually recombines in hundreds of picoseconds. The latter is clearly demonstrated by the fact that beyond 1 ps the spectra lose their intensity but do not change their spectral shape (see also dynamics in Supplementary Fig. 13).

These results show that for MAPbBr$_3$ as well, it is not possible to asses a unique value for the exciton binding energy, which will depend on the thin film morphology. Thus, optoelectronic devices made of large MAPbBr$_3$ crystals, with a stable excitonic population at room temperature, will work in a manner different to those made of thin films with a higher degree of polycrystallinity.

The effect of the degree of polycrystallinity on exciton binding energy can be rationalized by considering the role of disorder in such hybrid systems, with particular emphasis on the orientational order of the organic cation within the material. Large perovskite crystals (~1 µm in size) show a cooperative ordered phase of the organic cations that affects their rotational degrees of freedom[9,36]. This is not intrinsically related to the size of the crystal, but to the 'quality' of the crystallization process. We have shown recently that the crystallization process does affect the optoelectronic properties through modulation of the lattice strain[8,13]. Raman analysis[9,29] on the meso phase of MAPbI$_3$ (Supplementary Fig. 14) suggests a more distorted structural arrangement, so dipoles in the small crystals might be more randomly oriented within the inorganic cage. Of course, this can be induced by different factors, for example, the

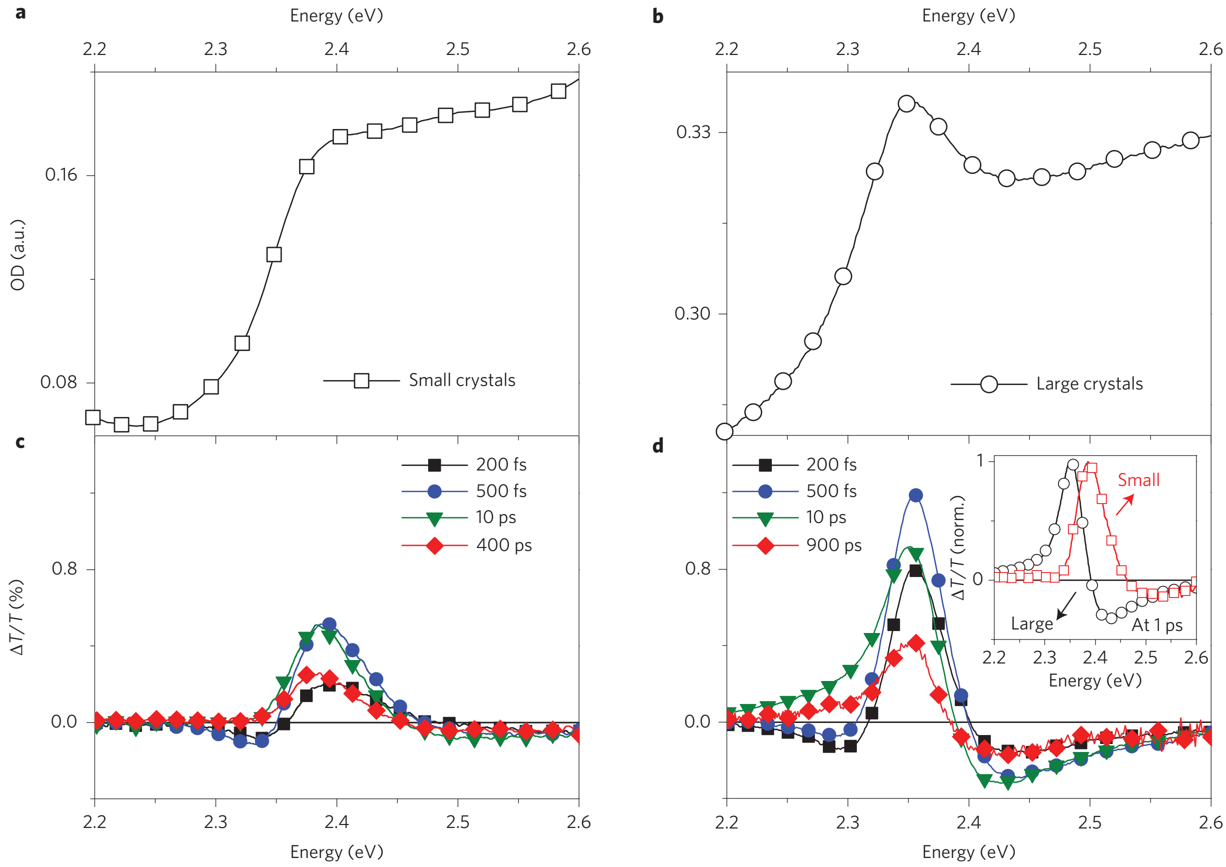

Figure 3 | Photo-induced excited population of MAPbBr$_3$ as a function of crystal size. UV–vis absorption spectra from MAPbBr$_3$ films with average crystallite dimension of ≪100 nm (**a**) and ∼1 μm (**b**). **c**,**d**, TA spectra at different time delays, at room temperature, from samples with small (**c**) and large (**d**) crystallites (for SEM images see Supplementary Fig. 12). Inset (**d**): comparison of TA spectra at 1 ps of small and large MAPbBr$_3$ crystals. For all TA measurements, the excitation wavelength is at 3.1 eV with an excitation density of $\sim 1 \times 10^{17}$ cm^{-3}.

crystallization procedure, the presence of dangling bonds on the surface, or the influence of external agents.

The organic cation has a permanent dipole moment, generating an electrostatic potential gradient that has the ability to influence electron–hole separation. If free to rotate, the dipoles will respond in a dielectric manner. This increases the low-frequency (hundreds of gigahertz) dielectric constant up to 35 (refs 37,38) in MAPbI$_3$. The Mott–Wannier exciton binding energy can be written as $E_b = (m^* e^4)/(\hbar^2 \varepsilon^2)$. If we take the optical frequency dielectric constant ($\varepsilon \approx 5$) this value is 45 meV, with an effective exciton Bohr radius of 4 nm. The binding energy is in very good agreement with the experimental value of ~50 meV (ref. 12). However, this model is valid only if the Coulomb interaction between the electron and hole is strong enough (and thus the kinetic energy of the small exciton high enough) that the slower lattice dielectric response does not screen the interaction. If the exciton is less strongly bound, we must consider also the low-frequency component of the dielectric constant arising from the lattice contributions. This would result in the exciton sampling a higher dielectric constant, thus decreasing its binding energy (up to 2 meV) and increasing the size (up to 19 nm), eventually dissociating it. To see how the different screening regimes are linked to the crystallization process we consider the microscopic effect of disorder and temperature by sampling the electrostatic potential resulting from simulating monocrystalline and polycrystalline films. We describe the changes in electrostatic potential on moving from a large grain to microcrystalline structure by extending a Monte Carlo procedure based on a model Hamiltonian parameterized for MAPbI$_3$ (ref. 39). The grain boundaries are induced by incorporating inactive lattice sites ('point defects') in the simulation (at densities of 6% and 10%), which enforces polycrystallinity within the simulation domains. The standard deviation in the electrostatic potential is plotted as a function of temperature and defect density (degree of polycrystallinity) in Fig. 4a, and representative domain structures and associated electrostatic potentials are shown in Fig. 4b–d.

For the monocrystalline system, the standard deviation in the electrostatic potential drops to zero with decreasing temperature. All the rotational disorder of the organic cations is quenched, leading to complete order and the formation of fully twinned domains. Disorder grows with temperature, as would be expected from statistical mechanics, generating increasing electrostatic potential variance. We note that this is in agreement with a recent work published by Miyata *et al.*, which reports an increase in the exciton binding energy with a reduction in temperature[16]. At room temperature, the electrostatic potential is fairly disordered, with a standard deviation of 163 meV, and the degree of polycrystallinity matters less at the level of defect density considered as all samples are thermally disordered. At lower temperatures, however, the variation in electrostatic potential is proportional to the degree of polycrystallinity and does not disappear at 0 K for the polycrystalline films (explicit tetragonal–orthorhombic phase transitions are not treated by the model). The largest variation in electrostatic potential occurs at grain boundaries, where the dipole twinning is disrupted (Fig. 4b–d; dipole alignments are represented in different morphologies and temperatures). These simulations confirm an interesting trend, that the variance of the electrostatic potential (that is local screening) can be controlled by the local order within the crystal. With larger, less defective crystals the variance is minimized. Thus, electron–hole separation

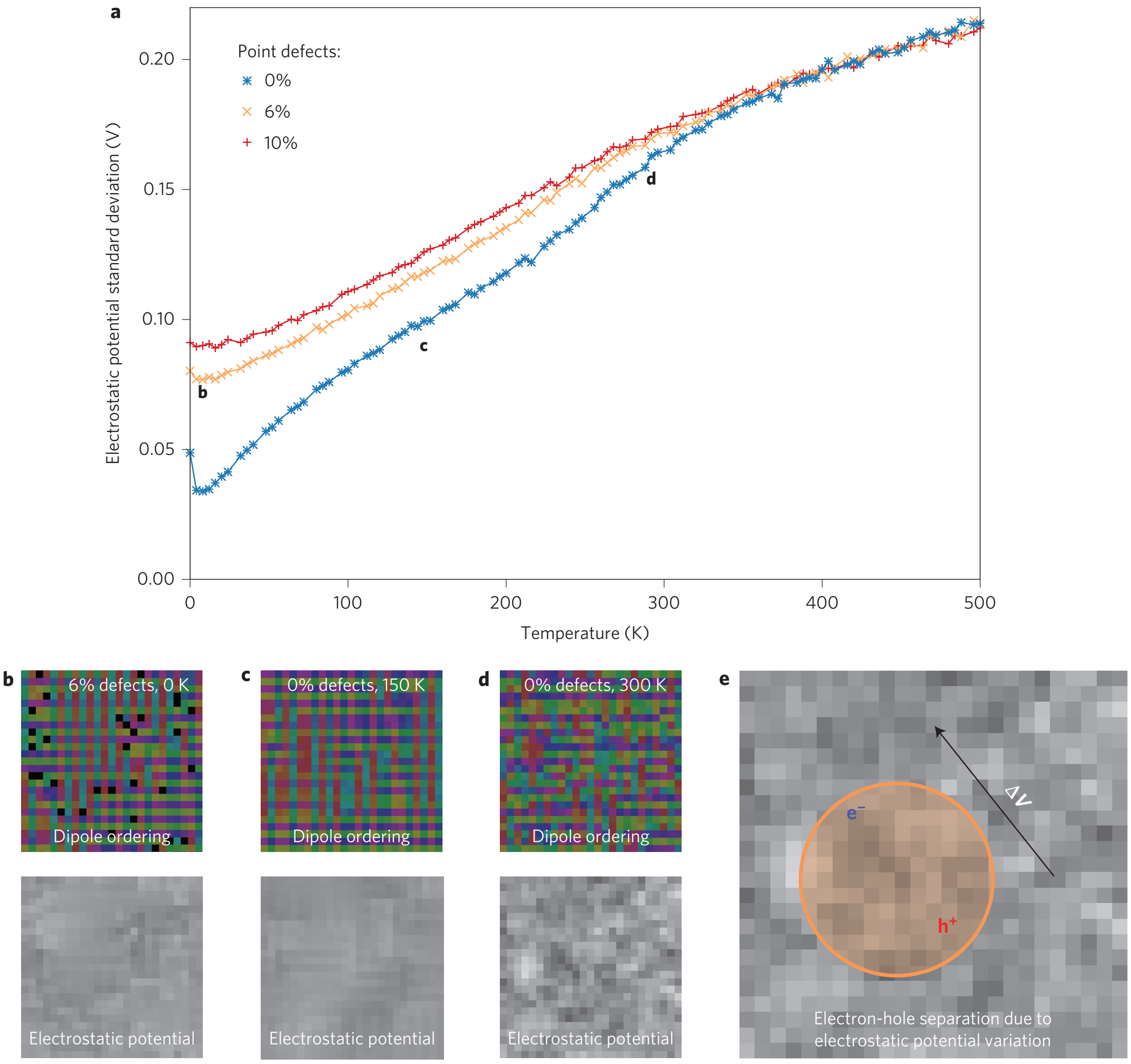

Figure 4 | Multiscale numerical Monte Carlo simulations of dipole alignment in methylammonium lead iodide. **a**, Standard deviation of electrostatic potential in Starrynight simulations of 250 × 250 interacting dipoles (150 × 150 nm crystallite), as a function of temperature. The standard variation in electrostatic potential for defect-free perovskite crystals (blue) decays and reduces to zero with a decrease in temperature. The 6% point defects (orange) and 10% point defects (red) trends show that there is non-vanishing disorder in the electrostatic potential, even at zero temperature. **b–d**, Small excerpts (25 × 25) of the simulation showing both dipole alignment (top panels) by pixel hue and the resulting electrostatic potential (bottom panels). Pure domains at 0 K are highly ordered in a columnar antiferroelectric alignment, leading to a smooth electrostatic potential (**b**), whereas defective crystals at 0 K contain electrostatic potential disorder as a result of frustrated alignment of the domains at the point defects (**c**). Room-temperature domains (**d**) show that thermal disorder at room temperature leads to a mostly paraelectric phase, with considerable electrostatic potential variance. **e**, Schematic representation of electron–hole interaction driven by electrostatic potential fluctuations. In samples where there is considerable electrostatic potential variation, the exciton will not be stable.

due to electrostatic disorder should be significant in small crystals (countering the Coulomb attraction between electrons and holes) but weaker in large crystals (allowing for Wannier exciton formation).

A single-crystal sample should represent the ultimate case study for our model. However, as mentioned earlier, discrepancies can be found in the literature with regard to the optical properties of such a sample[17,18]. Indeed, we have observed that a single crystal can show energetic dishomogeneity within surface and bulk phases with respect to the optical gap, following the same trend as the small and large crystallites (Supplementary Fig. 15). This can be understood from the presence of defects and fluctuations at the crystal termination, as we have theoretically predicted. The surface of the single crystal is an extended defect and it should be considered as comparable to the sample made of small crystallites. Due to the high absorbance of the single crystal, the absorption spectra presented in the literature have been measured through reflectivity[17,18], which is more sensitive to the surface than the bulk of the semiconductor. Thus, according to our model, we do not expect to see excitonic features. On the other hand, we have noticed that the EQE spectra (which may be more sensitive to the bulk properties of the semiconductor) of solar cells embodying a single crystal of $MAPbI_3$ show a defined exciton-like peak at the band-edge, in contrast to polycrystalline thin-film-based devices[18]. This observation suggests the strengthening of an excitonic transition, at room temperature, in the bulk of the single crystal, as we predict.

We can therefore conclude that the sensitivity of the molecular order to crystal quality, defects, as well as induced strain and device history, implies that there is considerable scope in the material processing to tune the nature and dynamics of the photophysical mechanisms characterizing each sample. Control of the dynamic polarization effect, which can provide both free-carrier and excitonic regimes for a single material composition, may open up a plethora of novel optoelectronic applications.

Methods

Methods and any associated references are available in the online version of the paper.

Received 26 January 2015; accepted 13 July 2015;
published online 17 August 2015

References

1. Zhou, H. *et al.* Interface engineering of highly efficient perovskite solar cells. *Science* **345,** 542–546 (2014).
2. Jeon, N. J. *et al.* Compositional engineering of perovskite materials for high-performance solar cells. *Nature* **517,** 476–480 (2015).
3. Xing, G., Mathews, N., Lim, S. & Yantara, N. Low-temperature solution-processed wavelength-tunable perovskites for lasing. *Nature Mater.* **13,** 476–480 (2014).
4. Deschler, F. *et al.* High photoluminescence efficiency and optically pumped lasing in solution-processed mixed halide perovskite semiconductors. *J. Phys. Chem. Lett.* **5,** 1421–1426 (2014).
5. Zhu, H. *et al.* Lead halide perovskite nanowire lasers with low lasing thresholds and high quality factors. *Nature Mater.* **14,** 636–642 (2015).
6. Tan, Z.-K. *et al.* Bright light-emitting diodes based on organometal halide perovskite. *Nature Nanotech.* **9,** 687–692 (2014).
7. Ball, J. M., Lee, M. M., Hey, A. & Snaith, H. J. Low-temperature processed meso-superstructured to thin-film perovskite solar cells. *Energy Environ. Sci.* **6,** 1739–1743 (2013).
8. De Bastiani, M., D'Innocenzo, V., Stranks, S. D., Snaith, H. J. & Petrozza, A. Role of the crystallization substrate on the photoluminescence properties of organo-lead mixed halides perovskites. *APL Mater.* **2,** 081509 (2014).
9. Grancini, G. *et al.* The impact of the crystallization processes on the structural and optical properties of hybrid perovskite films for photovoltaics. *J. Phys. Chem. Lett.* **5,** 3836–3842 (2014).
10. Marchioro, A. *et al.* Unravelling the mechanism of photoinduced charge transfer processes in lead iodide perovskite solar cells. *Nature Photon.* **8,** 250–255 (2014).
11. Manser, J. S. & Kamat, P. V. Band filling with free charge carriers in organometal halide perovskites. *Nature Photon.* **8,** 737–743 (2014).
12. D'Innocenzo, V. *et al.* Excitons versus free charges in organo-lead tri-halide perovskites. *Nature Commun.* **5,** 3486 (2014).
13. D'Innocenzo, V., Srimath Kandada, A. R., De Bastiani, M., Gandini, M. & Petrozza, A. Tuning the light emission properties by band gap engineering in hybrid lead-halide perovskite. *J. Am. Chem. Soc.* **136,** 17730–17733 (2014).
14. Lin, Q., Armin, A., Nagiri, R. C. R., Burn, P. L. & Meredith, P. Electro-optics of perovskite solar cells. *Nature Photon.* **9,** 106–112 (2014).
15. Saba, M. *et al.* Correlated electron–hole plasma in organometal perovskites. *Nature Commun.* **5,** 5049 (2014).
16. Miyata, A. *et al.* Direct measurement of the exciton binding energy and effective masses for charge carriers in an organic–inorganic tri-halide perovskite. *Nature Phys.* **11,** 582–587 (2015).
17. Shi, D. *et al.* Low trap-state density and long carrier diffusion in organolead trihalide perovskite single crystals. *Science* **347,** 519–522 (2015).
18. Dong, Q. *et al.* Electron–hole diffusion lengths >175 μm in solution-grown $CH_3NH_3PbI_3$ single crystals. *Science* **347,** 967–970 (2015).
19. Nie, W. *et al.* High-efficiency solution-processed perovskite solar cells with millimeter-scale grains. *Science* **347,** 522–525 (2015).
20. Im, J.-H., Jang, I.-H., Pellet, N., Grätzel, M. & Park, N.-G. Growth of $CH_3NH_3PbI_3$ cuboids with controlled size for high-efficiency perovskite solar cells. *Nature Nanotech.* **9,** 927–932 (2014).
21. Xing, G. *et al.* Long-range balanced electron- and hole-transport lengths in organic–inorganic $CH_3NH_3PbI_3$. *Science* **342,** 344–347 (2013).
22. Varshni, Y. P. Temperature dependence of the energy gap in semiconductors. *Physica* **34,** 149–154 (1967).
23. Onoda-Yamamuro, N., Matsuo, T. & Suga, H. Calorimetric and IR spectroscopic studies of phase transitions in methylammonium trihalogenoplumbates (II). *J. Phys. Chem. Solids* **51,** 1383–1395 (1990).
24. Shimizu, M., Fujisawa, J.-I. & Ishi-Hayase, J. Influence of dielectric confinement on excitonic nonlinearity in inorganic–organic layered semiconductors. *Phys. Rev. B* **71,** 205306 (2005).
25. Hulin, D. *et al.* Well-size dependence of exciton blue shift in GaAs multiple-quantum-well structures. *Phys. Rev. B* **33,** 4389–4391 (1986).
26. Peyghambarian, N. *et al.* Blue shift of the exciton resonance due to exciton–exciton interactions in a multiple-quantum-well structure. *Phys. Rev. Lett.* **53,** 2433–2436 (1984).
27. Schmitt-Rink, S., Chemla, D. & Miller, D. Theory of transient excitonic optical nonlinearities in semiconductor quantum-well structures. *Phys. Rev. B* **32,** 6601–6609 (1985).
28. Wu, X., Trinh, M. T. & Zhu, X. Excitonic many-body interactions in two-dimensional lead iodide perovskite quantum wells. *J. Phys. Chem. C* **119,** 14714–14721 (2015).
29. Quarti, C., Grancini, G. & Mosconi, E. The raman spectrum of the $CH_3NH_3PbI_3$ hybrid perovskite: interplay of theory and experiment. *J. Phys. Chem. Lett.* **5,** 279–284 (2014).
30. Even, J. *et al.* Solid-state physics perspective on hybrid perovskite semiconductors. *J. Phys. Chem. C* **119,** 10161–10177 (2015).
31. Heo, J. H., Song, D. H. & Im, S. H. Planar $CH_3NH_3PbBr_3$ hybrid solar cells with 10.4% power conversion efficiency, fabricated by controlled crystallization in the spin-coating process. *Adv. Mater.* **26,** 8179–8183 (2014).
32. Edri, E., Kirmayer, S., Cahen, D. & Hodes, G. High open-circuit voltage solar cells based on organic–inorganic lead bromide perovskite. *J. Phys. Chem. Lett.* **4,** 897–902 (2013).
33. Tanaka, K. *et al.* Comparative study on the excitons in lead-halide-based perovskite-type crystals $CH_3NH_3PbBr_3CH_3NH_3PbI_3$. *Solid State Commun.* **127,** 619–623 (2003).
34. Hoke, E. T. *et al.* Reversible photo-induced trap formation in mixed-halide hybrid perovskites for photovoltaics. *Chem. Sci.* **6,** 613–617 (2014).
35. Sadhanala, A. & Deschler, F. Preparation of single-phase films of $CH_3NH_3Pb(I_{1-x}Br_x)_3$ with sharp optical band edges. *J. Phys. Chem. Lett.* **5,** 2501–2505 (2014).
36. Mosconi, E., Quarti, C., Ivanovska, T., Ruani, G. & De Angelis, F. Structural and electronic properties of organo-halide lead perovskites: a combined IR-spectroscopy and *ab initio* molecular dynamics investigation. *Phys. Chem. Chem. Phys.* **16,** 16137–16144 (2014).
37. Wasylishen, R., Knop, O. & Macdonald, J. Cation rotation in methylammonium lead halides. *Solid State Commun.* **56,** 581–582 (1985).
38. Poglitsch, A. & Weber, D. Dynamic disorder in methylammoniumtrihalogenoplumbates (II) observed by millimeter-wave spectroscopy. *J. Chem. Phys.* **87,** 6373 (1987).
39. Frost, J. M., Butler, K. T. & Walsh, A. Molecular ferroelectric contributions to anomalous hysteresis in hybrid perovskite solar cells. *APL Mater.* **2,** 081506 (2014).

Acknowledgements

The research leading to these results has received funding from the European Union Seventh Framework Programme (FP7/2007-2013) under grant agreement no. 604032 of the MESO project, under grant agreement 316494 (DESTINY), the EU Horizon 2020 Research and Innovation Programme under grant agreement no. 643238 (SYNCHRONICS) and from Fondazione Cariplo (project GREENS no. 2013-0656). J.M.F. is funded by the EPSRC (EP/K016288/ and EP/M009580/1), and A.W. is supported by the European Research Council (project no. 277757). The authors thank S. Neutzner for help with fs-TA experiments and W. Xu for help with sample preparation. The authors thank E.T. Hoke, E.R. Dohner and H. Karunadasa for discussions and for providing the single crystal. The authors thank L. Manna for discussions and access to the XRD facility.

Author contributions

G.G., A.R.S.K. and A.J.B. performed the transient absorption measurements. M.G. and M.D.B. prepared the samples and characterized them by SEM. S.M. performed XRD and SEM characterization. G.G., A.R.S.K., G.L. and A.P. analysed the optical spectroscopy data. J.M.F. and A.W. performed the multiscale modelling and analysed the results. The manuscript was written with contributions from all authors. A.P. supervised the project.

Additional information

Supplementary information is available in the online version of the paper. Reprints and permissions information is available online at www.nature.com/reprints. Correspondence and requests for materials should be addressed to A.P.

Competing financial interests

The authors declare no competing financial interests.

Methods

Synthesis of methylammonium iodide salt. The precursor solution of perovskite was prepared following a well-established method reported in literature[1]. Methylamine solution (33 wt% in absolute ethanol, Sigma-Aldrich) was reacted with hydroiodic acid (57 wt% in water, Sigma-Aldrich) with excess methylamine in ethanol at 0 °C. Crystallization of CH_3NH_3I was achieved using a rotary evaporator. A white powder was formed, indicating successful crystallization. The salt was washed twice in diethyl ether to remove impurities.

Synthesis of methylammonium bromide salt. The solution was prepared as reported elsewhere[6] by adding methylamine solution (33 wt% in absolute ethanol, Sigma-Aldrich) and hydrobromic acid (48 wt% in water, Sigma-Aldrich) to 100 ml of absolute ethanol. The reaction mixture was stirred at 0 °C. The solvent was removed by rotary evaporation. The obtained white crystals were washed with anhydrous diethyl ether and recrystallized in ethanol. The perovskite precursor solution was prepared by mixing CH_3NH_3Br and $PbBr_2$ in a 1:1 molar ratio in anhydrous *N*,*N*-dimethylformamide to give concentrations of 20 and 5 wt%.

Preparation of samples for spectroscopy. All samples were prepared in a controlled nitrogen atmosphere either on glass microscope slides or on mesoporous Al_2O_3. To form mesoporous Al_2O_3, a commercial dispersion of alumina nanoparticles (20 wt% in isopropyl alcohol (IPA), average nanoparticle size of ~50 nm, Sigma-Aldrich) was spin-coated at 2,000 r.p.m. to form an ~3-μm-thick mesoporous layer, then dried at 150 °C for 30 min in air and for 10 min under an inert atmosphere.

To deposit $CH_3NH_3PbI_3$ on the mesoporous Al_2O_3, a hot (70 °C) solution of PbI_2 in DMF (dimethyl formamide, 0.5 M) was spin-coated at 2,000 r.p.m. for 60 s and subsequently annealed at 70 °C for 30 min. After cooling to room temperature, the substrate was dipped at room temperature in a CH_3NH_3I solution (0.063 M) in anhydrous IPA for 2 min. Samples were finally rinsed in anhydrous IPA to remove excess unreacted CH_3NH_3I.

The substrates were cleaned (two cycles of water, acetone and IPA in an ultrasonic bath for 10 min each) followed by oxygen plasma treatment for 10 min.

To deposit $CH_3NH_3PbI_3$ on glass, a hot (70 °C) solution of PbI_2 in DMF (1 M) was spin-coated at 2,000 r.p.m. for 60 s to obtain a 300-nm-thick layer. Subsequent annealing at 70 °C for 30 min was required to obtain the PbI_2 thin film. After cooling to room temperature, the substrate was dipped in a CH_3NH_3I solution in anhydrous IPA for 2 min. To obtain samples with different crystal sizes, the concentration and temperature of CH_3NH_3I was varied. To obtain films with ~100 nm crystals (Fig. 2a), the concentration was set at 0.063 M and the dipping was performed at room temperature, and to obtain crystals above 1 μm (Fig. 2b), the concentration was reduced to 0.045 M and the bath was warmed to 70 °C. The samples were finally rinsed in anhydrous IPA to remove excess unreacted CH_3NH_3I.

In the $CH_3NH_3PbBr_3$ one-step deposition method, CH_3NH_3Br and $PbBr_2$ were both dissolved in DMF (concentration of 20 wt% for deposition on the glass substrate and 10 wt% for deposition on the mesoporous alumina scaffold). The solution was spin-coated at 3,000 r.p.m. for 60 s. Subsequent annealing at 100 °C for 15 min was required to obtain the perovskite thin film.

Scanning electron microscopy. High-resolution scanning electron microscopy (HRSEM) was used to obtain the images in Fig. 1a,d. The samples were stuck on aluminium stubs with ultra-smooth double-sided adhesive tape, made of conductive carbon, specific for ultra high vacuum (UHV) systems and then coated with a 15 nm layer of conductive amorphous carbon. HRSEM observations were carried out using a JEOL JSM 7500FA scanning electron microscope, equipped with a cold field-emission gun (single-crystal tungsten ⟨310⟩ emitter, ultimate resolution of 1 nm) and operating at 10 kV.

The SEM images shown in Fig. 2 were collected using a high-vacuum tungsten filament commercial JEOL 6010-LV, with a working bias of 20 kV.

UV–visible absorption. Absorption spectra were recorded using a UV–vis–NIR spectrophotometer (PerkinElmer Lambda 1050 model) with a spectral range from 200 to 2,000 nm, with a resolution of ~1 nm.

Femtosecond transient absorption set-up. In a typical pump–probe experiment, the system under study was photoexcited by a short pump pulse (~120 fs) and its subsequent dynamical evolution was detected by measuring the transmission changes ΔT of a delayed probe pulse as a function of pump–probe delay and probe wavelength. The signal was given by the differential transmission $\Delta T/T = [(T_{\text{pump on}} - T_{\text{pump off}})/T_{\text{pump off}}]$. The system was driven by a mode-locked Ti:sapphire oscillator (Coherent Micra-18) operating at 80 MHz, used as a fundamental broadband source. This provided pulses with durations of ~20 fs and a central wavelength of 800 nm. A grating-based pulse stretcher (Coherent 9040) was used to temporally expand the pulses before amplification in a 250 kHz actively *Q*-switched Ti:sapphire-based regenerative amplifier (Coherent RegA 9000). The amplified pulses were subsequently temporally compressed in a grating-based compressor (Coherent 9040), resulting in pulses with temporal widths of ~35 fs and energies of ~6 μJ. A thin beamsplitter was used to split the amplified output into pump and probe beams. The pump beam was input into a two-pass collinear optical parametric amplifier (OPA) (Coherent 9450), allowing spectral conversion to any desired wavelength in the 480–750 nm wavelength range with resulting temporal broadening to ~120 fs. The probe beam was used for super-continuum generation within a sapphire plate, leading to probe pulses with significant continuous spectral content from 480 to 780 nm and temporal widths of ~100 fs. Both pump and probe pulses were focused and spatially overlapped in the sample space, with the temporal delay between them given by an optical retro-reflective delay line located on the pump arm of the system. Great care was taken to ensure that the spot size of the probe beam was significantly smaller than that of the pump beam. The resulting probe signal typically measured in transmission was coupled into an Acton SP2300i imaging spectrograph and the dispersed signal was measured by a custom (Stresing) silicon-based charge-coupled device linear array. The minimum detectable signal was $\Delta T/T \approx 10^{-5}$. The pump beam energy density used in the experiment was kept deliberately low (pump fluence of less than 1 μJ cm^{-2}, resulting in excitation densities on the order of 10^{17} cm^{-3}). All measurements were taken with the samples in a vacuum chamber to prevent any influence from oxygen or sample degradation. The temperature-dependent experiments were carried out using a continuous-flow static exchange gas cryostat (Oxford Instruments). The cryostat consisted of three chambers, one inside the other. The sample was housed inside the internal chamber, which was filled with gaseous nitrogen. The cryogenic liquid (N_2) was fluxed inside the second chamber, allowing temperature control of the N_2 atmosphere of the sample chamber. Eventually, a third chamber was evacuated (~10^{-5}–10^{-6} mbar) to ensure thermal isolation from the external ambient. A sensor close to the sample was mounted to accurately monitor the sample temperature.

Theoretical simulations. The Starrynight (molecular ferroelectric simulation) code[39] was adapted to model defective domains. Simulations were carried out in two dimensions with a 25 meV interaction between near-neighbour dipoles, no cage-strain term, a three-unit-cell cutoff for dipole interactions and periodic boundary conditions on a two-dimensional 250 × 250 grid. Strain (ordering) terms would be required to fully describe the tetragonal–orthorhombic phase transition and are expected to increase the order–disorder transition temperature of a phase, so the effective temperature reported in Fig. 4 may be considerably higher. The initial dipole orientation was random. A total of 10^5 Monte Carlo moves were attempted per site, with a Metropolis algorithm. The electrostatic potential variation was calculated from the sampled dipole orientation at equilibrium with a ten-unit-cell cutoff.